ACS Photonics
Article
pubs.acs.org/journal/apchd5

Large-Area and Ordered Sexfoil Pore Arrays by Spherical-Lens Photolithography

Chong Geng,[†] Qingfeng Yan,*[,†] Chengxiao Du,[‡] Peng Dong,[‡] Lijing Zhang,[†] Tongbo Wei,[‡] Zhibiao Hao,[§] Xiaoqing Wang,[†] and Dezhong Shen[†]

[†]Department of Chemistry, Tsinghua University, Beijing 100084, China
[‡]Institute of Semiconductors, Chinese Academy of Sciences, Beijing 100083, China
[§]Department of Electronic Engineering, Tsinghua University, Beijing 100084, China

ABSTRACT: Three-dimensional finite-difference time-domain simulation (FDTD), using both a single sphere model and a period model, were performed to study the size effect of colloidal spheres on the ordered pore array generated by spherical-lens photolithography (SLP). The size of the spheres ranged from just above the exposure wavelength to micron scale. A complex pattern consisting of a large and six surrounding tiny circular pores was obtained when the size of colloidal spheres increased to 2 μm, which was much different from the reported sole circular pore. The validation of simulation based on the period model was further verified by the experimental results. Large-area and ordered sexfoil pore arrays were observed when using 2 μm colloidal spheres monolayer as a microlens array. The slight difference between the simulation and the experiment results was attributed to the bleaching of the exposed photoresist. Sexfoil-shaped patterns have enriched the morphology of pore arrays generated by SLP, which may find applications in various technologically important areas.

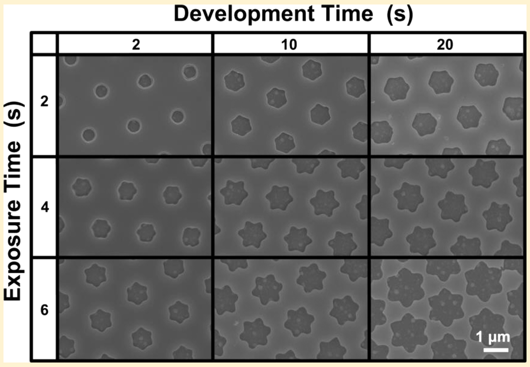

KEYWORDS: *spherical-lens photolithography, sexfoil pore arrays, colloidal crystal, FDTD simulation*

Ordered and periodic pore arrays have attracted a great deal of interests due to their wide applications in areas such as surface-plasmon resonance sensors,[1−4] photonic devices,[5,6] memberanes,[7−9] chemical sensors,[10−12] nanocontainers,[13−16] and biosensors.[17−19] A number of fabrication techniques including conventional photolithography,[20] focused-ion-beam lithography,[21,22] X-ray lithography,[23] electron-beam lithography,[24,25] nanoimprint lithography,[26,27] and UV-interference lithography[28] have been proposed. Although these approaches can be used to produce highly ordered pore arrays with uniform shape and size, either low-throughput or high-cost has limited their practical application especially in fabrication of large-area ordered pore arrays. Spherical-lens photolithography (SLP), first proposed by Wu et al.[29,30] and subsequently developed by other groups,[31−36] has been recognized as an inexpensive, inherently parallel, high-throughput approach to the creation of periodically ordered pore arrays with a large area. In a typical procedure, a monolayer of self-assembled colloidal spheres is deposited on a photoresist (PR) layer and serves as a lense array to focus the UV light to locally expose the PR. After development, a two-dimensional (2D) periodic pores array is formed on the PR. Consequently, the pore pattern can be transferred to the desired substrate beneath the PR layer for device construction by using wet/dry etching,[37−42] metal/dielectric deposition,[35,43] or selective area epitaxy.[44,45] Besides 2D periodic pore array, complex three-dimensional (3D) patterns could also be readily achieved by using SLP. Recently, Chang et al.[46] presented a 3D nanolithography process that utilized self-assembled nanospheres to create complex 3D nanosturctures by harnessing the Talbot field distribution generated by a 2D nanosphere array as a phase mask. Similary, Jeon et al.[47] reported a simple and cost-effective phase-shift lithography method for generating 3D nanostructures with a controlled lattice constant based on SLP.

For a 2D periodic pore array generated by SLP, it usually features a hexagonal pattern since the colloidal spheres generally arrange in hexagonal manner in a self-assembled monolayer. Few groups have reported the hole arrays other than hexagonal patterns. Recently, Bonakdar et al.[48] proposed a tilted exposure nanolithography technique to fabricate arrays of complex pore patterns with a wide range of geometrical configurations. The period of the pore array is directly related to the size of the colloidal sphere used. The size of pore is mainly determined by the sphere size but also affected by the exposure intensity and duration as well as the developing process. Thus, by manipulating the sphere size and processing conditions, ordered pore array with tunable pore size and period over large area can be obtained. One limitation for the pore array lies in that the shape of the pore is exclusively circular which is relatively monotonous. This kind of tedium in

Received: June 7, 2014
Published: August 1, 2014

dx.doi.org/10.1021/ph500203h | *ACS Photonics* 2014, 1, 754−760

pore shape, however, results in a constraint to study the shape-dependent properties of materials in case that, for example, the resultant pore array is used to produce surface-plasmon resonance devices. Recently, Asoh et al.[38] observed that a part of the SLP-generated pores appeared with a hexagonal shape. They attributed the appearance of the hexagonal contour of the pores to interference among adjacent microspheres during exposure, but no detailed evidence was provided.

The shape of the pores depends largely on the optical behavior of the microlens array upon focusing the incident UV light and exposuring the PR layer. During SLP, each colloidal sphere serves as a focusing lens. It is noteworthy that all colloidal spheres in the monolayer actually work simultaneously. Optical interference might occur between the focused light beams since the colloidal spheres are close-packed, leading to a more complex intensity distribution of the focused light in the PR layer. Apparently, such an effect correlates to the sphere size. Finite-difference time-domain (FDTD) method is one of the most common tools for simulating the optical behavior of microlens arrays. Several studies have investigated the intensity distribution of electromagnetic field inside a PR layer during SLP by using FDTD simulation with a single sphere as a model.[33,35,49] Although the single sphere model could evaluate the focusing ability of microlens easily, the interference among adjacent spheres is neglected during simulating. Recently, a few studies have selected a period as a model ato perform SLP FDTD simulation.[36,46] However, the size of the spheres used in these simulations was limited to submicron scale and only sole circular shaped pores were observed in these studies.

In the present work, 3D FDTD simulation was performed to study the size effect of the colloidal spheres on the size and shape of the ordered pore array generated by SLP. Both a single sphere model and a period model were employed to investigate the interference effect among adjacent microlens on the morphology of the pore array. The dimension of the spheres ranges from the nanoscale size just above the exposure wavelength (365 nm) to the micron scale size. It was found that a complex pattern consisting of a large and six surrounding tiny circles was obtained when the size of colloidal spheres increases, which is much different from the reported circular pore. The validation of simulation was further verified by the SLP experiment results. Sexfoil-shaped pore arrays were observed when using 2 μm colloidal spheres monolayer as a microlens array. The slight difference between the FDTD simulation and the experiment results is attributed to the bleaching of the exposed PR. Sexfoil-shaped patterns have enriched the morphology of pore arrays generated by SLP and may find applications in various technologically important areas.

■ EXPERIMENTAL SECTION

FDTD Simulations. Electromagnetic simulations were performed with the 3D FDTD method using a freely available software package.[50] The 3D computational domain involved a silicon substrate, a 500 nm photoresist layer (n = 1.4), PS monolayer colloidal crystal (MCC), and a thin air layer on top of the structure. Both a single sphere model and a period model were employed during simulation. For the period model, its rectangular unit cell is composed of a whole and six half spheres. The top and bottom boundaries were closed by perfectly matched layer, and periodic boundary conditions were applied at the side walls. The wavelength of the planar source corresponds to the i-line (365 nm). One planar monitor registered the light intensity at the interface between PS spheres and photoresist, and the other planar monitor was applied to record the cross sectional distribution of the electromagnetic field components.

Preparation of PS MCC. Monodisperse PS colloidal spheres of 420 nm, 900 nm, 1.5 μm, and 2 μm in diameter with a polydispersity less than 3% were synthesized using the emulsifier-free polymerization method.[51] The PS spheres were washed with DI water (resistivity up to 18.2 MΩ·cm, Ultra Pure UV, China) three times by repeated centrifugation and redispersed in DI water diluted with an equal volume of ethanol (99.95%, Sinopharm, China). PS monolayer colloidal crystal was fabricated by using the self-assembly approach at the air/water interface.[52−54] In a typical process, 10−20 μL of colloidal suspension were dropped on the water surface along the inside wall of a glass Petri dish (Φ = 8 cm). Once the suspension contacted the water, PS spheres spread rapidly onto the water surface. Due to the attractive capillary force and electrostatic repulsive force between charged colloidal spheres trapped at the air/water interface, self-assembly of the PS colloidal spheres took place. A drop of 2 wt % sodium dodecyl sulfonate (SDS, 98%, Sinopharm, China) aqueous solution, which could modify the water surface tension, was then added to consolidate the self-assembled colloidal arrays into a large-area close-packed monolayer.

Fabrication of Large-Area Ordered Pore Arrays via SLP. The fabrication procedure is schematically illustrated in Figure 1. After ultrasonic cleaning in isopropyl alcohol, Si substrates were rinsed with DI water and blow-dried by nitrogen. AR-P3120 PR (ALLRESIST, Germany) was spun-coated onto Si substrates at 5000 rpm for 40 s, and soft backed on a hot-plate at 100 °C for 5 min. Then Si substrates with photoresist were inserted beneath the floating MCC and lifted from water. The MCC self-assembled at the air/water interface was thus transferred onto the photoresist layer. Next, the

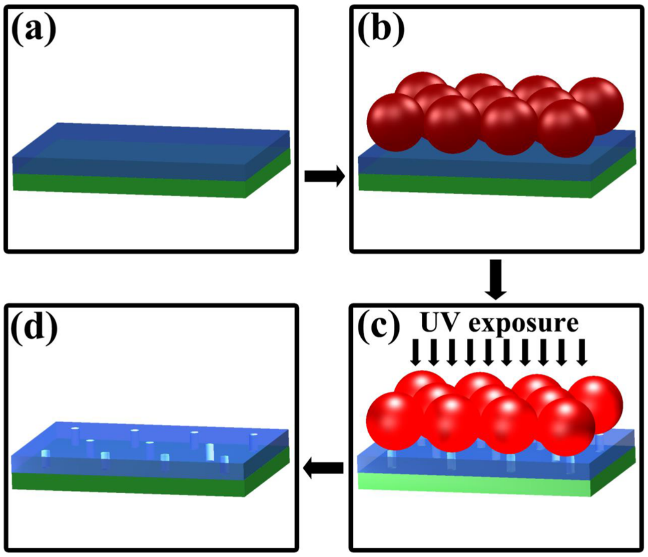

Figure 1. Schematic illustration of the process for the fabrication of periodic pore array via spherical-lens lithography: (a) photoresist spin-coated onto the silicon surface, (b) PS MCCs formed on top of the photoresist via the air/water interface self-assembly method, (c) UV light exposure of the photoresist covered by the PS MCC, and (d) photoresist with a subwavelength pore array pattern after development.

samples were UV exposed using a conventional photolithography instrument at a lamp power of about 10 mW/cm^2 and a center wavelength of 365 nm. After exposure, the substrates were immersed in DI water and sonicated for a few minutes to remove PS spheres. Finally, the samples were developed in AR 300−26 developer, followed by rinsing in DI water, and drying by nitrogen. Scanning electron microscope (SEM) images were obtained by a field-emission scanning electron microscope (Gemini LEO 1530). The samples were precoated with gold for 8 min using a sputter coater (Model 682, Gatan). The pressure was 6×10^{-4} Pa and the anode current was 100 μA. SEM images were captured at a working distance of 4−6 mm and a gun power of 10 kV.

■ RESULTS AND DISCUSSION

Results of the FDTD Simulations. The UV light propagation through PS spheres with different diameters was simulated by 3D-FDTD modeling method. The basic model for the simulation was a single PS sphere standing on top of the photoresist with a Si substrate below, and the surrounding was air, as shown in Figure 2a. *X* and *Y* axes ran perpendicularly through the sphere/PR contact point in the plane parallel with the substrate, and the *Z* axis was directed along the direction perpendicular to the substrate. During the simulations, the diameter of the spheres was the unique variable while keeping other conditions constant. Figure 2b shows the UV intensity of the focused light versus the position in the *X*−*Z* plane of the light's propagation with different diameters of PS spheres. It should be noted that the exposure intensity is a relative intensity and no unit is assigned. Considering an exposure intensity of 10 is the required intensity for a successful exposure, which is indicated as a dashed red line in Figure 2b, the size and depth of the well-exposed region both increase when spheres with a larger diameter are used. Thus, the focusing behavior of spheres becomes gradually stronger, with increasing diameter. Figure 2c,d illustrates the *X*−*Z* and *X*−*Y* views of the simulated time-averaging electromagnetic field energy distributions by using a 2 μm PS sphere as a microlens, respectively. The contour of the single sphere is highlighted by the white dotted circle, and the location of the interface between the sphere and PR is marked by the straight dotted line. The incident light collimates in a well-defined cylindrical shape inside the PR, demonstrating the focusing property of spheres during exposure.

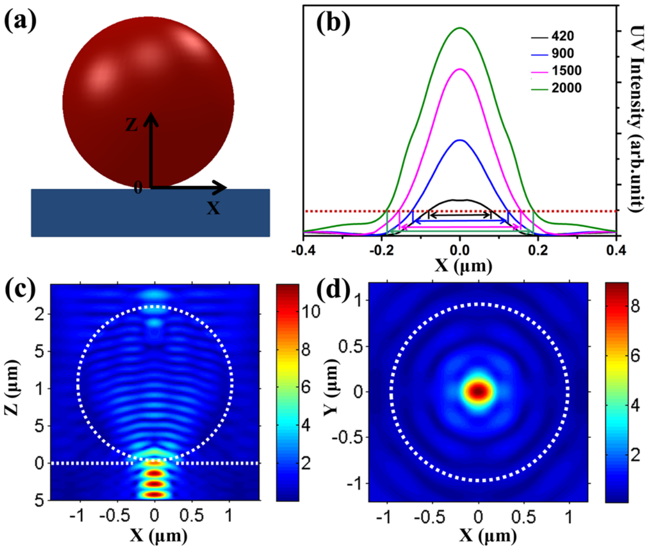

Figure 2. (a) Schematic of cross-section view of the single sphere model used for 3D FDTD simulation. (b) UV light intensity cross section after being focused by 2 μm PS sphere. (c) *X*−*Z* cut view and (d) *X*−*Y* cut view of the simulated time-averaging field energy distribution that demonstrates focusing the incident light by the single sphere of 2 μm in diameter.

The intensity distribution of the electromagnetic field is closely related to its surroundings. Considering the effect of the interference among adjacent spheres during exposure, a period consisting of was chosen as a model instead of a single sphere. Figure 3 shows the visualization and energy profile of the simulated intensity distribution within a period consisting of seven spheres. The cross-sectional monitor highlighted in green solid line in Figure 3a was to register the light intensity along the cross-sectional direction. The upper section in Figure 3b presents the tilted view of *X*−*Z* cut of the period model. For facilitating comparative analysis of the simulation results with that using a single sphere model, data bounded by the dotted line as shown in the lower section of Figure 3b was extracted.

The nanosphere with diameter of 420 nm which was just above exposure wavelength 365 nm could generate a focal spot appearing directly underneath the nanosphere, as shown in Figure 3c. This focusing behavior of nanosphere became gradually stronger with increasing the diameter from 420 to 900 nm, as shown in Figure 3d. However, the distribution of the light changed when the diameter of the spheres increased to 2 μm. Cross-sectional intensity distribution of 2 μm PS spheres shows two spots appear at the interface between PS spheres and photoresist, as indicated by the small solid circles in Figure 3e. *X*−*Y* cut time-averaging field energy distribution shown in Figure 3f demonstrates that six small light spots appeararound the large circular light spot underneath the sphere. The result is different from the only circular focal spot shown in Figure 2d, which utilized a single sphere as the simulation model. The occurrence of the six light spots can be ascribed to interference among adjacent spheres during exposure. Figure 3g visualizes the UV light intensity cross section when PS microsphere with different diameters was used. The collimated cylinder gets bigger and the depth-of-focus becomes deeper when increasing the size of spheres. When the diameter increased to 2 μm, two peaks appeared obviously on both sides of the main peak, as indicated by the two black arrows in Figure 3g.

Morphology of the Ordered Pore Arrays Generated by SLP Using PS Spheres of Different Diameters. Experimental verification of the above FDTD simulations was attempted by performing SLP using PS spheres with different diameters. Figure 4a−c shows SEM images of the resultant ordered pore arrays using 420 nm, 900 nm, and 2 μm spheres, respectively. The openings in the PR layer were obtained by developing 5 s after 6 s exposure.

A monolayer of PS spheres served as a lenses array during exposure. The intensity of focus light was several tens of times stronger than that of incident light, hence, resulting in site-selective exposure of the underlying PR layer. Information about the period of sphere array was transmitted to that of the pattern array, manifesting a one-to-one correspondence between spheres and pores. Thus, the period of the pore arrays in the PR was directly determined by the diameter of the spheres, and the period could be changed flexibly by varying the diameter of the spheres, as can be seen in Figure 4. While nanospheres with an average diameter of 420 nm resulted in a

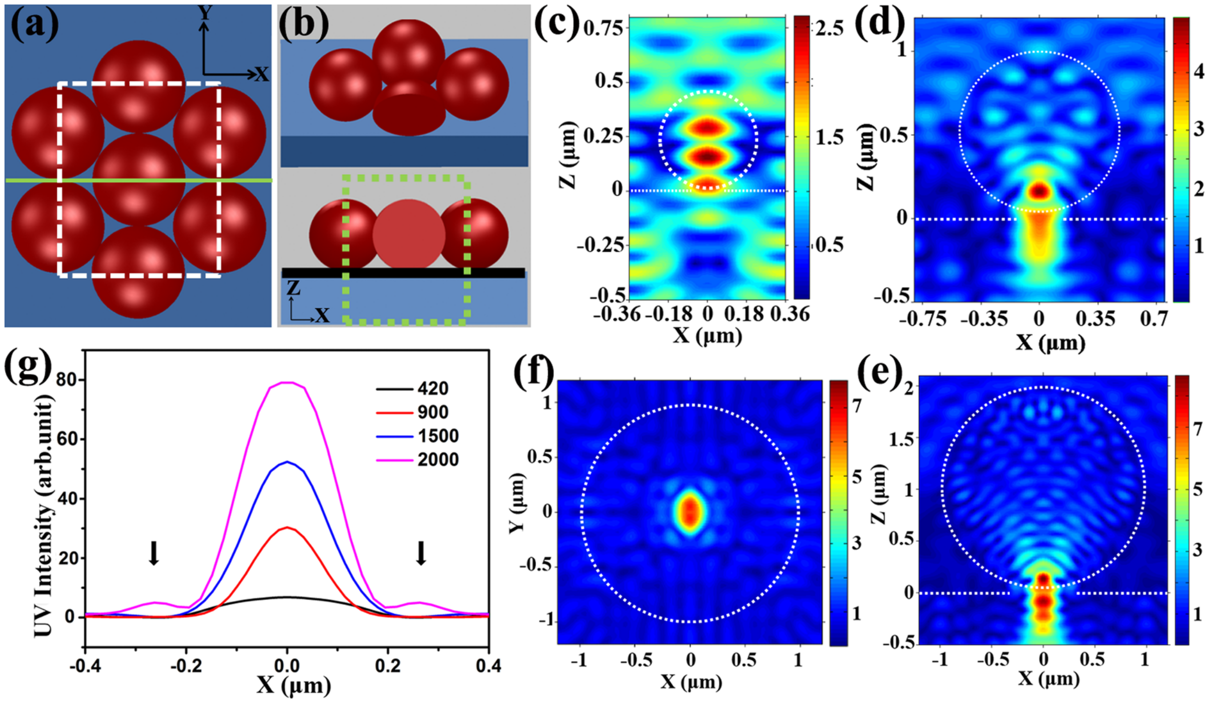

Figure 3. (a) A schematic illustration of the period model used for FDTD simulation and green line reprents the cross-sectional monitor. The single period is a rectangular unit cell highlighted by the dotted box, which is composed of a whole and six half spheres. (b) The tilt-veiw (top) and cross-sectional view (bottom) of $X-Z$ cut of the period model; The dotted box highlights the area from which the data are extracted. (c, d) Simulated time-averaging field energy distributions of 420 and 900 nm nanospheres, respectively. (e, f) $X-Z$ cut view and $X-Y$ cut view of the simulated time-averaging field energy distributions of 2 μm spheres, respectively. (g) The extracted energy profiles for spheres with various diameters when $x = 0.8$ μm.

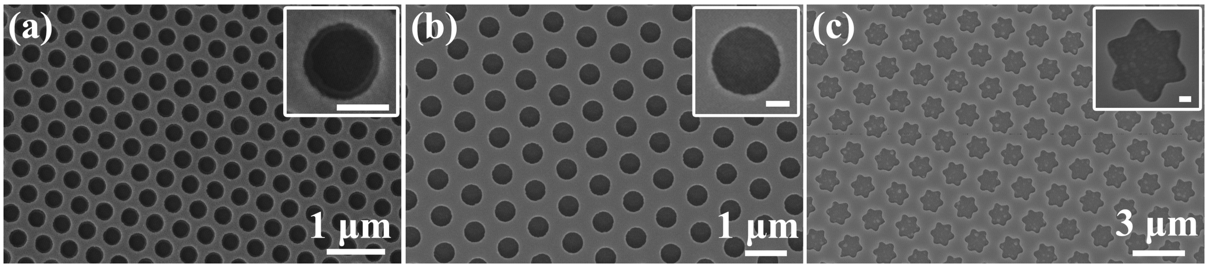

Figure 4. SEM images of ordered pore arrays fabricated by SLP using spheres with various diameters of (a) 420 nm, (b) 900 nm, and (c) 2 μm for the same exposure and development time. The insets are the corresponding magnified image of pore and the scale bars in the insets are all 200 nm.

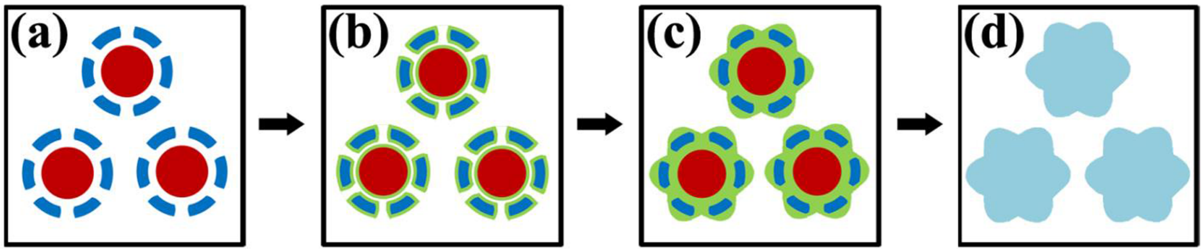

Figure 5. Schematic illustration of the sexfoil shape pore array during the exposure process.

nearly periodic pattern (Figure 4a), more definite and regular hexagonal arrangement of pores were observed with the diameter of 900 nm (Figure 4b). Furthermore, the insets shown in Figure 4a and b indicate that the contour of the pore is more circular in case larger PS spheres are used due to the improved focusing ability, as predicted by the FDTD simulation results with either a single sphere model or a period model.

With the diameter increasing to 2 μm, the shape of the opening appeared sexfoil (Figure 4c), which differed from the simulated result using the single sphere model shown in Figure 2d. However, the sexfoil shape looks like the pattern predicted by the FDTD simulation using the period model. The simulated result of the 2 μm spheres showed a complex pattern, consisting of a large circle and six tiny circles surrounding it (Figure 3f). The difference between the simulated and the experimental results could be ascribed to the bleaching of the photoresist, as schematically illustrated in Figure 5. Bleaching[55−58] is a description of the decrease in absorption of the photoresist after it is exposed. Therefore, in the beginning of the exposure, the photoresist along the propagation path of focused light was exposed first. With the exposure going on, the exposed domains in photoresist became partially transparent, laterally guiding light along the substrate and allowing a fuller exposure of the lateral photoresist. Both the big circle and the six tiny circles could act as the center of the bleaching, occurring radially in almost all directions. With the exposure going on, six tiny circle domains quickly contacted with the center large circle, resulting in the formation of the boundary line of the sexfoil.[59]

Effects of Process Conditions on the Morphology of Sexfoil Pore Array. The size of the sexfoil pores generated could be controlled by varying the exposure time and the development time. SEM images of ordered sexfoil pore arrays on the PR obtained with 2 μm spheres at different exposure and development times are shown in Figure 6. The size of the sexfoil shape is defined as the diameter of its inscribed circle, and the corresponding sizes of the sexfoil pores displayed in Figure 6 are listed in Table 1.

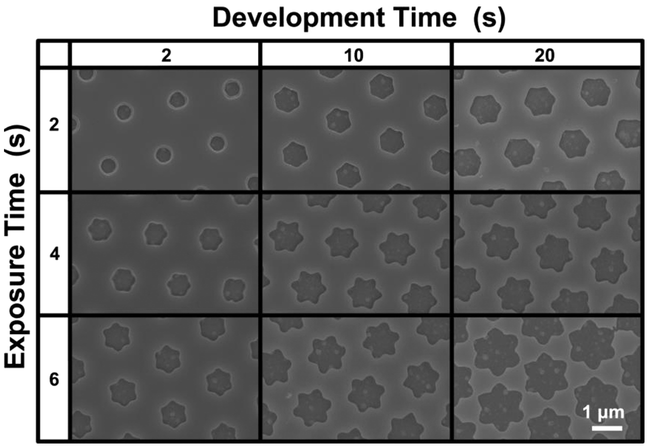

Figure 6. SEM images of uniform sexfoil pore arrays generated by SLP using 2 μm PS spheres with different exposure time and development time.

Table 1. Size Evolution of the Sexfoil Pores Obtained at Different Exposure and Development Time

exposure time (s)	development time (s)	avg diameter (nm)
2	2	526
	10	796
	20	945
4	2	726
	10	942
	20	1050
6	2	810
	10	1010
	20	1320

Comparing SEM images in each column of Figure 6, a phenomenon that the size of the pore increased with the exposure time when the development time was fixed could be observed. When the development time was fixed at 2 s, the sizes of the pores were 526, 726, and 810 nm, respectively. Attributing to the bleaching effect of PR, a larger region underneath the PS spheres could absorb sufficient photo energy to be developed. Therefore, the size of the sexfoil pores could be controlled by manipulating the exposure time.

Similarly, the size of the pores could be controlled by varying the development time with the constant exposure time. It is known that the exposure dose is a function of UV light irradiation multiplied by the exposure time. Moreover, the development rate decreased with lowering the exposure dose to a certain extent.[60] There is a strong evidence that the enlarging rate of the pores exposed for 6 s (31 nm/s) is obviously faster than that of the samples exposed for 2 s (14.9 nm/s) when extending the development time from 10 to 20 s. Therefore, the edge region with lower exposure dose took more time to develop as shown in SEM images in each row of Figure 6.

■ CONCLUSION

In summary, both a single sphere model and a period model were employed to study the optical behaviors of the microlens array during spherical-lens photolithography by using 3D FDTD simulation. The diameter of the spheres ranged from the size just above the exposure wavelength to the size in micron scale. When the diameter of the PS spheres used for light focusing increased to 2 μm, the 3D FDTD simulation using the period model predicted a focused pattern consisting of a large and six surrounding tiny circles. The phenomenon was ascribed to the interference among adjacent spheres during exposure, which was neglected in the conventional 3D FDTD simulation using the single-sphere model. The validation of simulation was approved by comparing the simulation results with the experiment results. The period of the ordered pore array was changed flexibly by varying the diameter of the spheres. Large-area ordered sexfoil-shaped pore arrays were obtained by SLP using 2 μm sphere as microlens. The bleaching of the exposed PR led to the difference between the simulation results and the experiment results. By manipulating the exposure time and the development time, the size of the sexfoil pores could be easily tuned. Sexfoil-shaped pore arrays observed in this study enrich the micro/nanostructures generated by spherical-lens photolithography. Combining with other techniques, array of sexfoil pores may find many potential applications in nano/microfabrication area by serving as a mask for deposition, etching or site-selective epitaxy. For example, the metallic sexfoil disk array produced using the sexfoil pore array as a deposition mask might possess interesting plasmonic properties comparing with the conventional metallic circular disk array.

■ AUTHOR INFORMATION

Corresponding Author

*E-mail: yanqf@mail.tsinghua.edu.cn.

Notes

The authors declare no competing financial interest.

■ ACKNOWLEDGMENTS

The authors would like to thank the financial support from the National Key Basic Research Program of China (No. 2013CB632900) and the National Science Foundation of China (Nos. 51173097 and 91333109). The Tsinghua University Initiative Scientific Research Program, the Tsinghua National Laboratory for Information Science and Technology (TNList) Cross-Discipline Foundation, and the State Key

Laboratory of New Ceramics and Fine Processing, Tsinghua University, are also acknowledged for partial financial support.

■ REFERENCES

(1) Brolo, A. G.; Gordon, R.; Leathem, B.; Kavanagh, K. L. Surface plasmon sensor based on the enhanced light transmission through arrays of nanoholes in gold films. *Langmuir* **2004**, *20*, 4813−4815.

(2) Brolo, A. G.; Kwok, S. C.; Moffitt, M. G.; Gordon, R.; Riordon, J.; Kavanagh, K. L. Enhanced fluorescence from arrays of nanoholes in a gold film. *J. Am. Chem. Soc.* **2005**, *127*, 14936−14941.

(3) Saboktakin, M.; Ye, X.; Chettiar, U. K.; Engheta, N.; Murray, C. B.; Kagan, C. R. Plasmonic enhancement of nanophosphor upconversion luminescence in au nanohole arrays. *ACS Nano* **2013**, *7*, 7186−7192.

(4) Hall, A. S.; Friesen, S. A.; Mallouk, T. E. Wafer-scale fabrication of plasmonic crystals from patterned silicon templates prepared by nanosphere lithography. *Nano Lett.* **2013**, *13*, 2623−2627.

(5) Liguda, C.; Böttger, G.; Kuligk, A.; Blum, R.; Eich, M.; Roth, H.; Kunert, J.; Morgenroth, W.; Elsner, H.; Meyer, H. Polymer photonic crystal slab waveguides. *Appl. Phys. Lett.* **2001**, *78*, 2434−2436.

(6) Menezes, J. W.; Ferreira, J.; Santos, M. J.; Cescato, L.; Brolo, A. G. Large-area fabrication of periodic arrays of nanoholes in metal films and their application in biosensing and plasmonic-enhanced photovoltaics. *Adv. Funct. Mater.* **2010**, *20*, 3918−3924.

(7) Yan, F.; Goedel, W. A. Polymer Membranes with two-dimensionally arranged pores derived from monolayers of silica particles. *Chem. Mater.* **2004**, *16*, 1622−1626.

(8) Wan, L.-S.; Li, J.-W.; Ke, B.-B.; Xu, Z.-K. Ordered microporous membranes templated by breath figures for size-selective separation. *J. Am. Chem. Soc.* **2011**, *134*, 95−98.

(9) Lu, Z.-X.; Namboodiri, A.; Collinson, M. M. Self-supporting nanopore membranes with controlled pore size and shape. *ACS Nano* **2008**, *2*, 993−999.

(10) Hong, G.; Li, C.; Qi, L. Facile fabrication of two-dimensionally ordered macroporous silver thin films and their application in molecular sensing. *Adv. Funct. Mater.* **2010**, *20*, 3774−3783.

(11) Jia, L.; Cai, W.; Wang, H.; Sun, F.; Li, Y. Hetero-apertured micro/nanostructured ordered porous array: layer-by-layered construction and structure-induced sensing parameter controllability. *ACS Nano* **2009**, *3*, 2697−2705.

(12) Lai, X.; Wang, D.; Han, N.; Du, J.; Li, J.; Xing, C.; Chen, Y.; Li, X. Ordered arrays of bead-chain-like In_2O_3 nanorods and their enhanced sensing performance for formaldehyde. *Chem. Mater.* **2010**, *22*, 3033−3042.

(13) Yuan, J.; Qu, L.; Zhang, D.; Shi, G. Linear arrangements of polypyrrole microcontainers. *Chem. Commun.* **2004**, 994−995.

(14) Tian, T.; LeJeune, Z. M.; Garno, J. C. Directed surface assembly of 4-(chloromethyl) phenyltrichlorosilane: self-polymerization within spatially confined sites of Si (111) viewed by atomic force microscopy. *Langmuir* **2013**, *29*, 6529−6536.

(15) Liu, C.; Liu, J.; Gao, D.; Ding, M.; Lin, J.-M. Fabrication of microwell arrays based on two-dimensional ordered polystyrene microspheres for high-throughput single-cell analysis. *Anal. Chem.* **2010**, *82*, 9418−9424.

(16) Li, X.; Zhang, L.; Wang, Y.; Yang, X.; Zhao, N.; Zhang, X.; Xu, J. A bottom-up approach to fabricate patterned surfaces with asymmetrical TiO_2 microparticles trapped in the holes of honeycomblike polymer film. *J. Am. Chem. Soc.* **2011**, *133*, 3736−3739.

(17) Simon, A.; Girard-Egrot, A.; Sauter, F.; Pudda, C.; Picollet D'Hahan, N.; Blum, L.; Chatelain, F.; Fuchs, A. Formation and stability of a suspended biomimetic lipid bilayer on silicon submicrometer-sized pores. *J. Colloid Interface Sci.* **2007**, *308*, 337−343.

(18) Kleefen, A.; Pedone, D.; Grunwald, C.; Wei, R.; Firnkes, M.; Abstreiter, G.; Rant, U.; Tampé, R. Multiplexed parallel single transport recordings on nanopore arrays. *Nano Lett.* **2010**, *10*, 5080−5087.

(19) Hotta, K.; Yamaguchi, A.; Teramae, N. Nanoporous waveguide sensor with optimized nanoarchitectures for highly sensitive label-free biosensing. *ACS Nano* **2012**, *6*, 1541−1547.

(20) Martin, O. J. Surface plasmon illumination scheme for contact lithography beyond the diffraction limit. *Microelectron. Eng.* **2003**, *67*, 24−30.

(21) Silverman, J. P. X-ray lithography: status, challenges, and outlook for 0.13 mm. *J. Vac. Sci. Technol., B* **1997**, *15*, 2117−2124.

(22) Ito, T.; Okazaki, S. Pushing the limits of lithography. *Nature* **2000**, *406*, 1027−1031.

(23) Melngailis, J.; Mondelli, A.; Berry, I. L., III; Mohondro, R. A review of ion projection lithography. *J. Vac. Sci. Technol., B* **1998**, *16*, 927−957.

(24) Corbierre, M. K.; Beerens, J.; Lennox, R. B. Gold nanoparticles generated by electron beam lithography of gold(I)-thiolate thin films. *Chem. Mater.* **2005**, *17*, 5774−5779.

(25) Ebbesen, T. W.; Lezec, H.; Ghaemi, H.; Thio, T.; Wolff, P. Extraordinary optical transmission through sub-wavelength hole arrays. *Nature* **1998**, *391*, 667−669.

(26) Chou, S. Y.; Krauss, P. R.; Renstrom, P. J. Nanoimprint lithography. *J. Vac. Sci. Technol., B* **1996**, *14*, 4129−4133.

(27) Guo, L. J. Nanoimprint lithography: methods and material requirements. *Adv. Mater.* **2007**, *19*, 495−513.

(28) Prenen, A. M.; Van Der Werf, J.; Bastiaansen, C. W.; Broer, D. J. Monodisperse, polymeric nano- and microsieves produced with interference holography. *Adv. Mater.* **2009**, *21*, 1751−1755.

(29) Wu, H.; Odom, T. W.; Whitesides, G. M. Generation of chrome masks with micrometer-scale features using microlens lithography. *Adv. Mater.* **2002**, *14*, 1213−1216.

(30) Wu, M.-H.; Paul, K. E.; Whitesides, G. M. Patterning flood illumination with microlens arrays. *Appl. Opt.* **2002**, *41*, 2575−2585.

(31) Wu, W.; Dey, D.; Memis, O. G.; Katsnelson, A.; Mohseni, H. A novel self-aligned and maskless process for formation of highly uniform arrays of nanoholes and nanopillars. *Nanoscale Res. Lett.* **2008**, *3*, 123−127.

(32) Wu, W.; Katsnelson, A.; Memis, O. G.; Mohseni, H. A deep sub-wavelength process for the formation of highly uniform arrays of nanoholes and nanopillars. *Nanotechnology* **2007**, *18*, 485302−485305.

(33) Wu, W.; Dey, D.; Memis, O. G.; Katsnelson, A.; Mohseni, H. Fabrication of large area periodic nanostructures using nanosphere photolithography. *Nanoscale Res. Lett.* **2008**, *3*, 351−354.

(34) Wu, W.; Dey, D.; Katsnelson, A.; Memis, O. G.; Mohseni, H. Large areas of periodic nanoholes perforated in multistacked films produced by lift-off. *J. Vac. Sci. Technol., B* **2008**, *26*, 1745−1747.

(35) Chang, Y.-C.; Chung, H.-C.; Lu, S.-C.; Guo, T.-F. A large-scale sub-100 nm Au nanodisk array fabricated using nanospherical-lens lithography: A low-cost localized surface plasmon resonance sensor. *Nanotechnology* **2013**, *24*, 095302.

(36) Szabó, Z.; Volk, J.; Fülöp, E.; Deák, A.; Bársony, I. Regular ZnO nanopillar arrays by nanosphere photolithography. *Photon. Nanostruct.* **2013**, *11*, 1−7.

(37) Hou, C.-H.; Tseng, S.-Z.; Chan, C.-H.; Chen, T.-J.; Chien, H.-T.; Hsiao, F.-L.; Chiu, H.-K.; Lee, C.-C.; Tsai, Y.-L.; Chen, C.-C. Output power enhancement of light-emitting diodes via two-dimensional hole arrays generated by a monolayer of microspheres. *Appl. Phys. Lett.* **2009**, *95*, 133105−133107.

(38) Asoh, H.; Iwata, J.; Ono, S. Hexagonal geometric patterns formed by radial pore growth of InP based on voronoi tessellation. *Nanotechnology* **2012**, *23*, 215304−215311.

(39) Vlad, A.; Frölich, A.; Zebrowski, T.; Dutu, C. A.; Busch, K.; Melinte, S.; Wegener, M.; Huynen, I. Direct transcription of two-dimensional colloidal crystal arrays into three-dimensional photonic crystals. *Adv. Funct. Mater.* **2013**, *23*, 1164−1171.

(40) Dong, P.; Yan, J.; Wang, J.; Zhang, Y.; Geng, C.; Wei, T.; Cong, P.; Zhang, Y.; Zeng, J.; Tian, Y. 282-nm AlGaN-based deep ultraviolet light-emitting diodes with improved performance on nano-patterned sapphire substrates. *Appl. Phys. Lett.* **2013**, *102*, 241113−241116.

(41) Ono, S.; Kotaka, S.; Asoh, H. Fabrication and structure modulation of high-aspect-ratio porous GaAs through anisotropic

chemical etching, anodic etching, and anodic oxidation. *Electrochim. Acta* **2013**, *110*, 393−401.

(42) Asoh, H.; Fujihara, K.; Ono, S. Triangle pore arrays fabricated on Si (111) substrate by sphere lithography combined with metal-assisted chemical etching. *Nanoscale Res. Lett.* **2012**, *7*, 406−413.

(43) Chang, Y.-C.; Wang, S.-M.; Chung, H.-C.; Tseng, C.-B.; Chang, S.-H. Observation of absorption-dominated bonding dark plasmon mode from metal−insulator−metal nanodisk arrays fabricated by nanospherical-lens lithography. *ACS Nano* **2012**, *6*, 3390−3396.

(44) Wei, T.; Wu, K.; Lan, D.; Yan, Q.; Chen, Y.; Du, C.; Wang, J.; Zeng, Y.; Li, J. Selectively grown photonic crystal structures for high efficiency InGaN emitting diodes using nanospherical-lens lithography. *Appl. Phys. Lett.* **2012**, *101*, 211111−211115.

(45) Du, C.; Wei, T.; Zheng, H.; Wang, L.; Geng, C.; Yan, Q.; Wang, J.; Li, J. Size-controllable nanopyramids photonic crystal selectively grown on P-GaN for enhanced light-extraction of light-emitting diodes. *Opt. Express* **2013**, *21*, 25373−25380.

(46) Chang, C.-H.; Tian, L.; Hesse, W.; Gao, H.; Choi, H.; Kim, J.-G.; Siddiqui, M.; Barbastathis, G. From two-dimensional colloidal self-assembly to three-dimensional nanolithography. *Nano Lett.* **2011**, *11*, 2533−2537.

(47) Jeon, T. Y.; Jeon, H. C.; Lee, S. Y.; Shim, T. S.; Kwon, J. D.; Park, S. G.; Yang, S. M. 3D hierarchical architectures prepared by single exposure through a highly durable colloidal phase mask. *Adv. Mater.* **2013**, *26*, 1422−1426.

(48) Bonakdar, A.; Jang, S. J.; Mohseni, H. Novel high-throughput and maskless photolithography to fabricate plasmonic molecules. *J. Vac. Sci. Technol. B* **2014**, *32*, 020604.

(49) Wu, W.; Katsnelson, A.; Memis, O. G.; Mohseni, H. A deep sub-wavelength process for the formation of highly uniform arrays of nanoholes and nanopillars. *Nanotechnology* **2007**, *18*, 485302.

(50) Oskooi, A. F.; Roundy, D.; Ibanescu, M.; Bermel, P.; Joannopoulos, J. D.; Johnson, S. G. Meep: A flexible free-software package for electromagnetic simulations by the FDTD method. *Comput. Phys. Commun.* **2010**, *181*, 687−702.

(51) Shim, S. E.; Cha, Y. J.; Byun, J. M.; Choe, S. Size control of polystyrene beads by multistage seeded emulsion polymerization. *J. Appl. Polym. Sci.* **1999**, *71*, 2259−2269.

(52) Yu, J.; Yan, Q.; Shen, D. Co-self-assembly of binary colloidal crystals at the air−water interface. *ACS Appl. Mater. Interfaces* **2010**, *2*, 1922−1926.

(53) Li, C.; Hong, G.; Wang, P.; Yu, D.; Qi, L. Wet chemical approaches to patterned arrays of well-aligned ZnO nanopillars assisted by monolayer colloidal crystals. *Chem. Mater.* **2009**, *21*, 891−897.

(54) Geng, C.; Zheng, L.; Yu, J.; Yan, Q.; Wei, T.; Wang, X.; Shen, D. Thermal annealing of colloidal monolayer at the air/water interface: A facile approach to transferrable colloidal masks with tunable interstice size for nanosphere lithography. *J. Mater. Chem.* **2012**, *22*, 22678−22685.

(55) Chen, C.; Sun, X.; Zhang, D.; Shan, Z.; Shin, S.-Y.; Zhang, D. Dye-doped polymeric planar waveguide devices based on a thermal UV-bleaching technique. *Opt. Laser Technol.* **2009**, *41*, 495−498.

(56) Wang, X.-B.; Sun, J.; Chen, C.-M.; Sun, X.-Q.; Wang, F.; Zhang, D.-M. Thermal UV treatment on Su-8 polymer for integrated optics. *Opt. Mater. Exp.* **2014**, *4*, 509−517.

(57) Henderson, C.; Pancholi, S.; Chowdhury, S.; Willson, C.; Dammel, R. *Photoresist Characterization for Lithography Simulation. Part 2: Exposure Parameter Measurements*; SPIE proceedings series; International Society for Optics and Photonics, SPIE: Bellingham, WA, 1997; pp 816−828.

(58) Henderson, C. L.; Willson, C. G.; Dammel, R. R.; Synowicki, R. A. *Bleaching-Induced Changes in the Dispersion Curves of DNQ Photoresists, Microlithography '97*; International Society for Optics and Photonics, SPIE: Bellingham, WA, 1997; pp 585−595.

(59) Erdmann, A.; Henderson, C. L.; Willson, C. G. Impact of Exposure Induced Refractive Index Changes of Photoresists on the Photolithographic Process. *J. Appl. Phys.* **2001**, *89*, 8163−8168.

(60) Jakatdar, N. H.; Niu, X.; Spanos, C. J. *Characterization of a Chemically Amplified Photoresist for Simulation Using a Modified Poor Man's Drm Methodology*; 23rd Annual International Symposium on Microlithography; International Society for Optics and Photonics, SPIE: Bellingham, WA, 1998; pp 578−585.